APPLIED PHYSICS

Programmable nonreciprocal Poynting effect enabled by lattice metamaterials

Le Dong[1,2], Kun Zhou[3], Dong Wang[1,2]*

Shear nonreciprocity, implying unequal shear forces in opposite shear directions, can be achieved by arranging structures asymmetrically. However, the nonreciprocal Poynting effect, i.e., unequal normal stresses induced by the same shear displacements to the left and right, has not been fully explored. We discover the nonreciprocal Poynting effect using a generalized directional truss model. Inspired by this discovery, the cylindrical lattice metamaterials constructed from antisymmetric curled microstructures are used as a case study to generate the nonreciprocal Poynting effect. We develop a design framework that integrates digital generation, finite deformation theory, finite element modeling, and three-dimensional printing to program the nonreciprocal Poynting effect. Applications such as bionic Poynting effect matching, wave energy converter, and unidirectional motion limitation are demonstrated. This framework allows the one-to-one mapping between the torque and normal forces, paving the way for designing soft devices with precise force transmission capabilities.

INTRODUCTION

Reciprocity is a fundamental principle of transmission in numerous physical systems. It means that signal propagation through the system always occurs in a symmetric manner, thus ensuring that the system responds equally to inputs from opposite directions (*1*, *2*). Recently, there has been a growing interest in breaking the symmetry of signal transmission in both temporal and spatial dimensions to induce nonreciprocal behaviors, mainly in dynamic systems involving electromagnetic (*3*–*5*), acoustic (*6*–*8*), and mechanical (*9*–*13*) wave propagation. Static nonreciprocity introduces a unique ability to manipulate mechanical signals and energy without requiring active time-modulated components (*14*–*18*). For example, Coulais *et al.* (*14*) broke the Maxwell-Betti reciprocity theorem with a fishbone metamaterial, revealing static shear nonreciprocity. Wang *et al.* (*16*) proposed a composite hydrogel with intrinsic shear nonreciprocity achieved by incorporating directionally embedded nanofillers.

An important nonlinear phenomenon observed during simple shear is the Poynting effect (*19*), i.e., the shear-induced normal stress in the direction perpendicular to the shear plane. Note that the Poynting effect differs from the compression-twisting effect. Although both phenomena involve longitudinal and transverse displacements, the displacements are driven by the normal force in the compression-twisting effect (*20*, *21*) and by the shear force in the Poynting effect (*22*, *23*). Traditionally, the Poynting effect demonstrates that the normal stress remains the same when shearing in both the left and right directions (*24*–*27*), which is reciprocal and adheres to the Maxwell-Betti reciprocity theorem (*1*) ($F_{\mathrm{R}}^{\perp}U = F_{\mathrm{L}}^{\perp}U$ in Fig. 1A). Similar to the formation of nonreciprocal shear, a nonreciprocal Poynting effect arises when this theorem is violated, leading to unequal normal stresses for identical shear displacements to the left and right ($F_{\mathrm{R}}^{\perp}U \neq F_{\mathrm{L}}^{\perp}U$ in Fig. 1B).

The nonreciprocal Poynting effect exists in both nature and engineering. An example is the myocardium's different normal stress responses when shearing to the left and right directions (*28*). This effect is also suggested by the directional microstructures in various biological tissues (*29*). In materials engineering, the asymmetric normal stresses induced from shearing fiber-aligned materials can cause different elastic instabilities, complicating the manufacturing process (*30*, *31*). Thus, understanding this effect is crucial for accurately simulating or compensating for the uneven normal forces for biological applications, such as developing high-fidelity surgical simulators (*32*), as well as for the efficient execution of manufacturing processes. Furthermore, the nonreciprocal Poynting effect can be induced from torsion, which enables the design of cylindrical soft devices with both load-bearing and precise force transmission capabilities (*33*, *34*). However, systematic exploration of the nonreciprocal Poynting effect remains limited. Preliminary theoretical research has identified the first-order term in the normal force for fiber-reinforced materials under simple shear, confirming the effect's existence (*35*, *36*). By understanding its formation mechanism and developing theoretical models, we can gain quantitative insights and enhance its applications.

In this work, we have introduced a general truss model to illustrate the formation mechanism of the nonreciprocal Poynting effect. The truss model also reveals that the material nonlinearity can be used to tune the magnitudes of the nonreciprocal Poynting effect. Inspired by this discovery, cylindrical lattice metamaterials consisting of curled microstructures are used as a case study to generate the nonreciprocal Poynting effect. Curled microstructures are used to tune the nonlinear stress-strain behaviors. A design framework for the cylindrical lattice metamaterials is developed to program the nonreciprocal Poynting effect, which integrates digital generation, finite deformation modeling, finite element (FE) simulations, and three-dimensional (3D) printing fabrication. The finite deformation model establishes the relationship between the Poynting effect and geometric and material parameters. On the basis of the design framework, various Poynting effects with programmable magnitudes are designed. The applications of the nonreciprocal Poynting effect such as bionic Poynting effect matching, wave energy converter, and unidirectional motion limiter are demonstrated. This work allows one-to-one mapping between the torque and normal forces, enabling the design of soft devices for direct force transmission.

[1]State Key Laboratory of Mechanical System and Vibration, School of Mechanical Engineering, Shanghai Jiao Tong University, Shanghai 200240, China. [2]Meta Robotics Institute, Shanghai Jiao Tong University, Shanghai 200240, China. [3]Singapore Centre for 3D Printing, School of Mechanical and Aerospace Engineering, Nanyang Technological University, 50 Nanyang Avenue, Singapore 639798, Singapore.
*Corresponding author. Email: wang_dong@sjtu.edu.cn

RESULTS

Nonreciprocal Poynting effect by the truss model

A directional truss system consisting of two inclined trusses constrained by two plates is used to illustrate the formation mechanism of the nonreciprocal Poynting effect (Fig. 1C). The incline angle is θ. The trusses can exhibit linear or nonlinear elastic behavior. When an identical shear deformation U is applied in the left or right direction (Fig. 1, D and E), the third-order Taylor expansions of the normal force $F_R^\perp$ (for right shearing) and $F_L^\perp$ (for left shearing) are calculated as

$$F_R^\perp = \eta_1^\perp (K_A - K_B)U + \eta_2^\perp (K_A + K_B)U^2 + \eta_3^\perp (K_A - K_B)U^3 + O(U^3) \quad (1)$$

$$F_L^\perp = -\eta_1^\perp (K_A - K_B)U + \eta_2^\perp (K_A + K_B)U^2 - \eta_3^\perp (K_A - K_B)U^3 + O(U^3) \quad (2)$$

where K_A and K_B are parameters that characterize the material stiffness of the two trusses. $\eta_i^\perp$ ($i = 1$ to 3) are coefficients to the ith order of U, which are dependent on θ. The detailed derivations and dimensionless setups can be found in sections S1 and S2. When the two trusses are identical ($K_A = K_B$), $F_R^\perp = F_L^\perp$ and the truss system exhibits a reciprocal Poynting effect.

When the two trusses are different ($K_A \neq K_B$), $F_R^\perp \neq F_L^\perp$ and the normal force difference is

$$\Delta F^\perp \equiv F_R^\perp - F_L^\perp = 2\eta_1^\perp (K_A - K_B)U + 2\eta_3^\perp (K_A - K_B)U^3 + O(U^3) \quad (3)$$

Thus, the nonreciprocal vertical phenomenon ($\Delta F^\perp \neq 0$) exists even for infinitesimal deformation when $K_A \neq K_B$. The higher-order terms contribute to the magnitude of the resultant normal force difference.

The effects of material nonlinearity and geometric parameters on the Poynting effect are investigated. Figure 2A shows the linear, Γ-shaped, and J-shaped stress-strain curves for the elastic trusses. $\eta_i^\perp$ ($i = 1$ to 3) of the linear, Γ-shaped, and J-shaped truss systems are calculated and given by eqs. S14, S18, and S19, respectively. Figure 2B plots $\eta_1^\perp$ and $\eta_2^\perp$ against the incline angle θ. The $\eta_1^\perp$ are the same as the initial tangent moduli are set the same for all three types of trusses. It can be observed that $\hat{\eta}_2^\perp > \eta_2^\perp > \breve{\eta}_2^\perp$, which can be attributed to the different nonlinear behaviors of the Γ-shaped and J-shaped curves. Here, the symbols $\hat{(\cdot)}$ and $\breve{(\cdot)}$ represent the corresponding parameters for the Γ-shaped and J-shaped truss systems, respectively.

Figure 2 (C to E) shows the normal force distributions for linear, Γ-shaped, and J-shaped nonlinear materials with varying θ and K_A/K_B under $U = 0.5$. The stress-strain curves of the trusses A and B have the same shape but with different magnitudes. Solid and dashed curves represent zero normal force contours when sheared to the right and left, respectively. These contours are determined by setting Eqs. 1 and 2 to zero. The resulting contours divide the normal forces into four regions: both left and right shear-induced normal forces are positive (++), both negative (−−), positive and negative (+−), and negative and positive (−+).

The intersection point of the two contours in the linear truss system (Fig. 2C) occurs at $K_A/K_B = 1$ and θ = 54.74°, indicating zero Poynting effect. As K_A/K_B increases, a nonreciprocal Poynting effect emerges with $F_L^\perp = -F_R^\perp < 0$. The nonreciprocal Poynting effect is observed with $F_L^\perp = -F_R^\perp > 0$ when K_A/K_B decreases. Figure 2F plots the change of the corresponding normal force with U for $K_A/K_B = 2$, 1, and 1/2 at θ = 54.74°.

From Eqs. 1 and 2, the second-order term has the same form $\eta_2^\perp (K_A + K_B)U^2$ for both $F_L^\perp$ and $F_R^\perp$. Thus, both $F_L^\perp$ and $F_R^\perp$ increase with $\eta_2^\perp$. For the Γ-shaped truss system, the "++" region is larger because $\hat{\eta}_2^\perp$ is the largest (Fig. 2D). Poynting effects in the ++ region

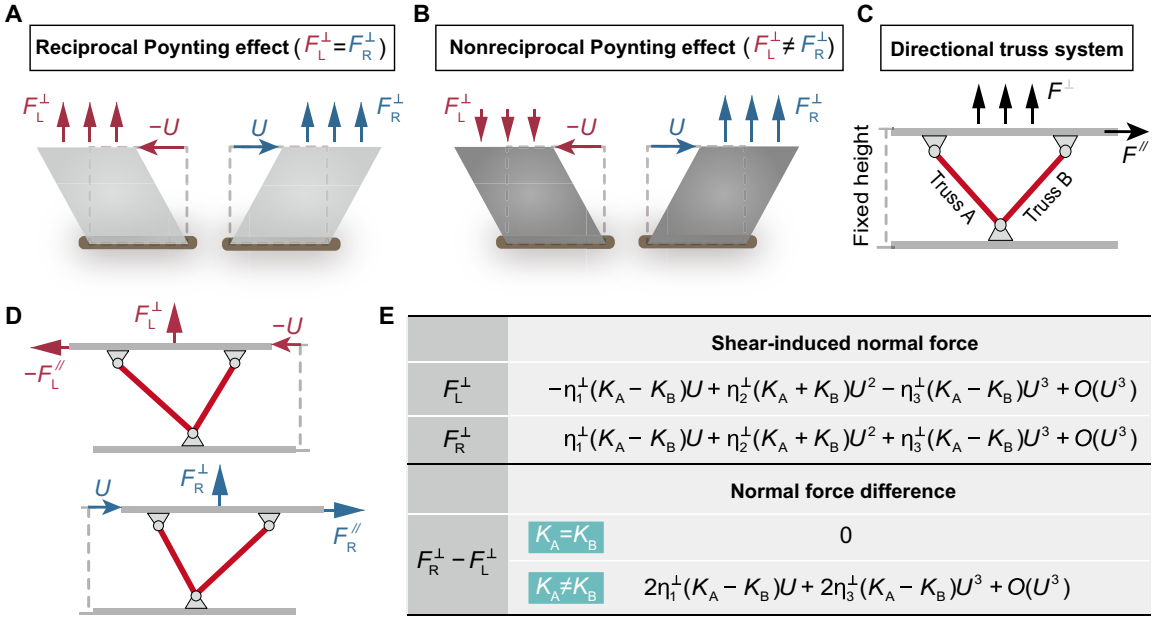

	Shear-induced normal force
$F_L^\perp$	$-\eta_1^\perp(K_A - K_B)U + \eta_2^\perp(K_A + K_B)U^2 - \eta_3^\perp(K_A - K_B)U^3 + O(U^3)$
$F_R^\perp$	$\eta_1^\perp(K_A - K_B)U + \eta_2^\perp(K_A + K_B)U^2 + \eta_3^\perp(K_A - K_B)U^3 + O(U^3)$
	Normal force difference
$F_R^\perp - F_L^\perp$ ($K_A = K_B$)	0
$F_R^\perp - F_L^\perp$ ($K_A \neq K_B$)	$2\eta_1^\perp(K_A - K_B)U + 2\eta_3^\perp(K_A - K_B)U^3 + O(U^3)$

Fig. 1. Nonreciprocal Poynting effect. (**A**) Reciprocal Poynting effect ($F_R^\perp U = F_L^\perp U$). (**B**) Nonreciprocal Poynting effect ($F_R^\perp U \neq F_L^\perp U$). (**C**) A directional truss system consists of two inclined trusses constrained by two plates. (**D**) Schematic of the resultant shear and normal forces when a shear deformation U is applied in the left or right direction. (**E**) The shear-induced normal force and resultant normal force difference under $K_A = K_B$ and $K_A \neq K_B$.

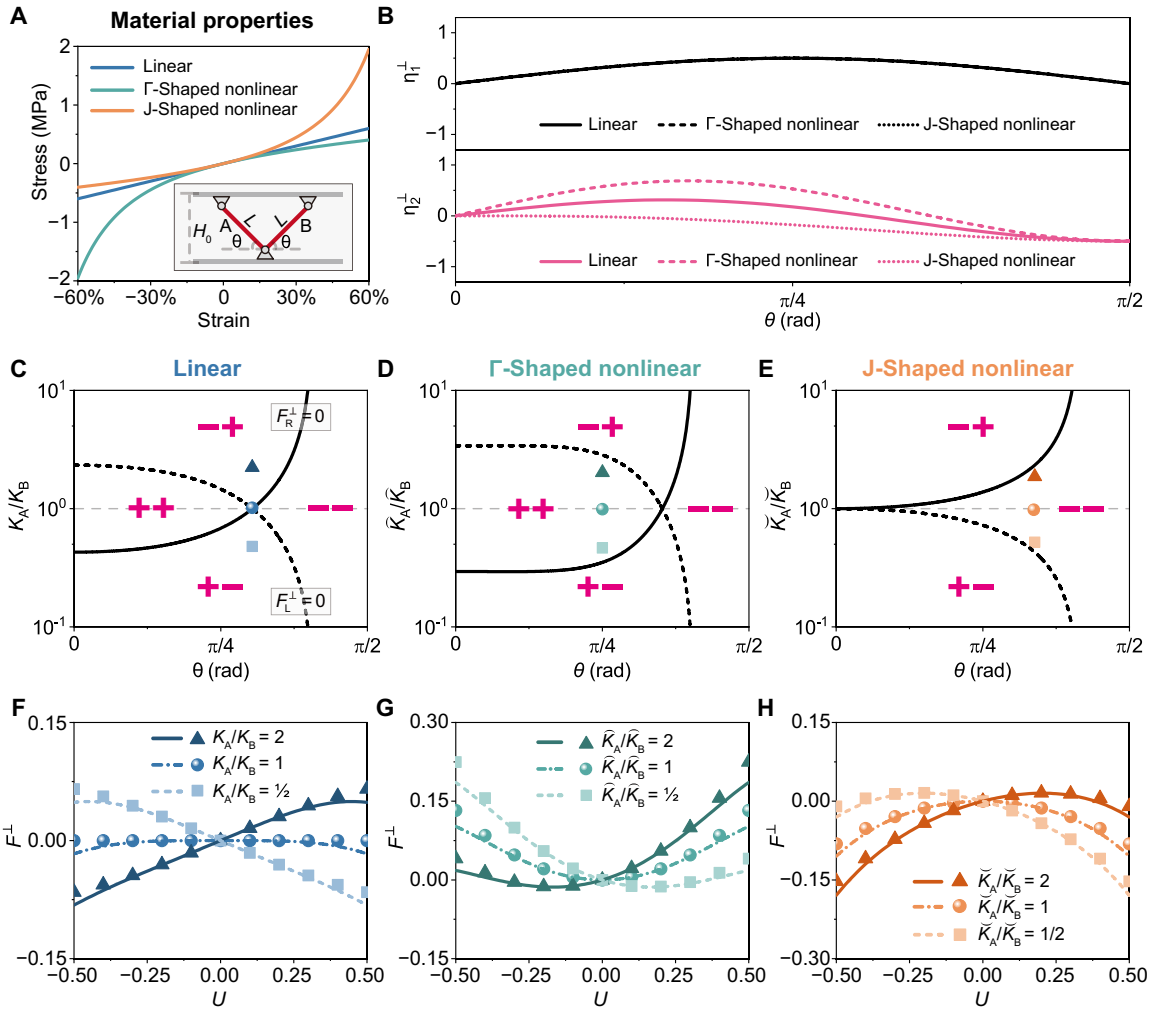

Fig. 2. Nonreciprocal Poynting effect tuned by K_A/K_B and θ. (**A**) Stress-strain curves for linear, Γ-shaped, and J-shaped elastic materials. (**B**) The dependences of $\eta_1^{\perp}$ and $\eta_2^{\perp}$ on θ. Normal force distributions for (**C**) linear, (**D**) Γ-shaped, and (**E**) J-shaped nonlinear materials with varying θ and K_A/K_B under $U = 0.5$. The solid and dashed curves represent zero normal force contours when sheared to the right and left, respectively. (**F** to **H**) The dependence of dimensionless normal force $F^{\perp}$ on U for different K_A/K_B and θ [as represented by the triangles, circles, and squares that appear in (C) to (E)]. The markers denote results from the third-order Taylor expansion, while the curves represent the exact values.

are all observed for $\widehat{K}_A/\widehat{K}_B = 2, 1$, and $^1/_2$ at $\theta = \pi/4$. $\widehat{K}_A/\widehat{K}_B = 1$ leads to a positive reciprocal Poynting effect (circles), while $F_R^{\perp} > F_L^{\perp} > 0$ at $\widehat{K}_A/\widehat{K}_B = 2$ (triangles) and $F_L^{\perp} > F_R^{\perp} > 0$ at $\widehat{K}_A/\widehat{K}_B = 1/2$ (squares) (Fig. 2G). Conversely, the ++ region diminishes as $\breve{\eta}_2^{\perp}$ is always negative for the J-shaped truss system (Fig. 2E). Negative Poynting effects are all observed with $\breve{K}_A/\breve{K}_B = 2, 1$, and $^1/_2$ at $\theta = \pi/3$. It can be observed that $F_L^{\perp} < F_R^{\perp} < 0$ for $\breve{K}_A/\breve{K}_B = 2$, $F_L^{\perp} = F_R^{\perp} < 0$ for $\breve{K}_A/\breve{K}_B = 1$, and $F_R^{\perp} < F_L^{\perp} < 0$ for $\breve{K}_A/\breve{K}_B = 1/2$ (Fig. 2H). The truss model is further extended to multi-segment vertical arrays to facilitate the programming of the Poynting effect. Two- and three-segment vertical arrays are theoretically studied (section S3).

Modeling of cylindrical lattice metamaterials

Inspired by the directional truss system, cylindrical lattice metamaterials are used as a case study to program the nonreciprocal Poynting effect. The cylindrical lattice metamaterial is formed by wrapping a periodic rectangular lattice into a cylindrical shape (Fig. 3A). The periodic unit comprises four antisymmetric curled microstructures indexed as I to IV. Instead of the straight trusses, curled microstructures are used to mimic the J-shaped stress-strain behaviors of the trusses due to the transition from bending-dominated to tension-dominated deformation (*37*, *38*). Microstructures are constructed using the curvature function $R(\alpha) = \alpha^n$ $(0 \le \alpha \le \alpha_{end})$ that defines the relationship between the instantaneous radius of curvature R and the slope angle α. The programmable J-shaped stress-strain curves can be obtained by tuning geometric parameters (fig. S7). Three different units are shown in Fig. 3B.

A theoretical model is developed to predict the Poynting effect of cylindrical lattice metamaterials. A torque T is applied on both ends. The resultant reaction force F needed to maintain the original height between the two ends is investigated. The normal force $F^{\perp}$ is equal to $-F$. A thin-walled cylindrical structure under torsion can be simplified as the unfolded planar structure under simple shear with deformation compatibility requirements (*39*). Figure 3C

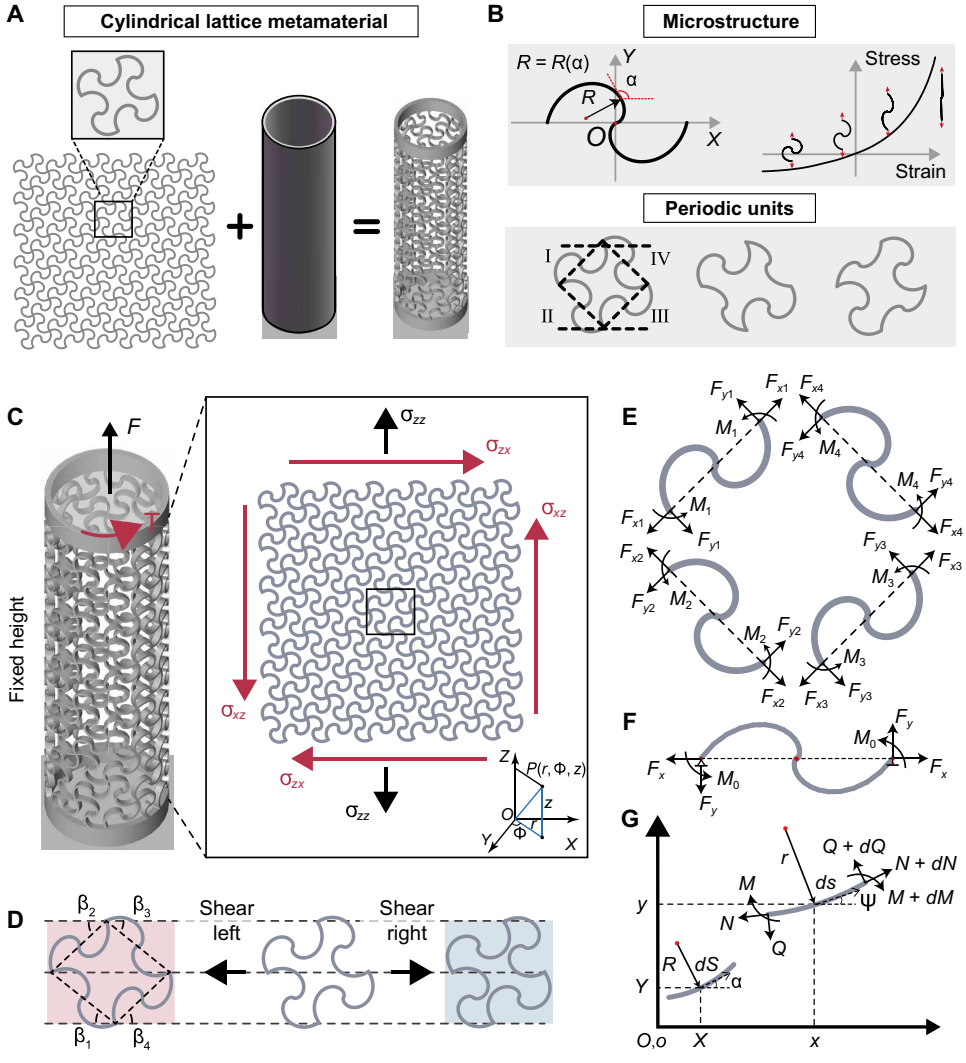

Fig. 3. Cylindrical lattice metamaterials enabled the nonreciprocal Poynting effect. (**A**) A cylindrical lattice metamaterial constructed by 6 × 6 periodic units. Each periodic unit is formed by four microstructures. (**B**) Curled microstructures with J-shaped stress-strain curves are constructed from the curvature functions. Three different units are shown. (**C**) The cylindrical lattice metamaterial under torsion T and reaction force F is simplified to a 2D lattice under vertical stress σ_{zz} and shear stress σ_{xz}. (**D**) The deformation of the periodic unit shearing to the left or right direction. (**E**) Inner forces and moments on each microstructure. (**F**) The microstructure is modeled as simply supported with the horizontal force F_x, vertical force F_y, and moment M_0 at both ends. (**G**) Inner forces and moments of an infinitesimal beam element before and after deformation.

shows the cylindrical lattice metamaterial under T and F and the corresponding planar structure under shear stress $\sigma_{xz}(\sigma_{xz} = \sigma_{zx})$ and normal stress σ_{zz}. The relationships between T and σ_{xz} and between F and σ_{zz} are

$$T = \int_{\frac{D-t}{2}}^{\frac{D+t}{2}} \int_{0}^{2\pi} \sigma_{xz} r^2 d\Phi dr = \left(\frac{D^2 t}{2} + \frac{t^3}{6} \right) \pi \sigma_{xz} \text{ and } F = \pi D t \sigma_{zz} \quad (4)$$

where D is the diameter of the cylindrical lattice metamaterials, t is the radial thickness, and Φ and r represent the angle and radius in cylindrical coordinates, respectively.

Consider a periodic unit consisting of four microstructures I to IV. The static equilibrium gives the relations between the inner forces and the external loading (Fig. 3E), which requires

$$\begin{pmatrix} \sin\beta_2 & \cos\beta_2 & 0 & 0 & 0 & 0 & \sin\beta_3 & -\cos\beta_3 \\ \cos\beta_2 & -\sin\beta_2 & 0 & 0 & 0 & 0 & -\cos\beta_3 & -\sin\beta_3 \\ \sin\beta_2 & \cos\beta_2 & -\sin\beta_1 & \cos\beta_1 & 0 & 0 & 0 & 0 \\ 0 & 0 & -\cos\beta_1 & -\sin\beta_1 & \cos\beta_4 & -\sin\beta_4 & 0 & 0 \\ 0 & 0 & 0 & 0 & \sin\beta_4 & \cos\beta_4 & -\sin\beta_3 & \cos\beta_3 \end{pmatrix} \begin{pmatrix} F_{x1} \\ F_{y1} \\ F_{x2} \\ F_{y2} \\ F_{x3} \\ F_{y3} \\ F_{x4} \\ F_{y4} \end{pmatrix} = \sqrt{2}Lt \begin{pmatrix} \sigma_{zz} \\ \sigma_{zx} \\ \sigma_{xz} \\ \sigma_{zx} \\ \sigma_{xz} \end{pmatrix} \quad (5)$$

The moment equilibrium of the joint connected by the four microstructures I to IV gives the following relation

$$\sum_{i=1}^{4} M_i = -\sum_{i=1}^{4} (F_{yi} L_i)/2 = 0 \quad (6)$$

where L and L_i are the undeformed and deformed lengths between two ends of the microstructures, and β_i characterizes the rigid-body motion of each microstructure. The angle between the tangent directions of two connected microstructures remains unchanged during deformation. Thus, we have

$$\begin{pmatrix} 1 & 1 & 0 & 0 \\ 0 & 1 & 1 & 0 \\ 1 & 0 & 0 & 1 \end{pmatrix}\begin{pmatrix} \beta_1 \\ \beta_2 \\ \beta_3 \\ \beta_4 \end{pmatrix}+\begin{pmatrix} 1 & -1 & 0 & 0 \\ 1 & 0 & 0 & -1 \\ 0 & -1 & 1 & 0 \end{pmatrix}\begin{pmatrix} \psi_1 \\ \psi_2 \\ \psi_3 \\ \psi_4 \end{pmatrix}=\begin{pmatrix} \frac{\pi}{2} \\ \frac{\pi}{2} \\ \frac{\pi}{2} \end{pmatrix} \tag{7}$$

where ψ_i ($i = 1$ to 4) is the tangent angle at the end of each microstructure. The deformation compatibility requires that the side lengths and interior angles of the deformed rectangle satisfy the following geometric relations

$$\begin{pmatrix} \sin\beta_2 & \sin\beta_1 & -\sin\beta_4 & -\sin\beta_3 \\ \cos\beta_2 & -\cos\beta_1 & -\cos\beta_4 & \cos\beta_3 \\ \sin\beta_2 & 0 & 0 & -\sin\beta_3 \\ \sin\beta_2 & \sin\beta_1 & 0 & 0 \end{pmatrix}\begin{pmatrix} L_1 \\ L_2 \\ L_3 \\ L_4 \end{pmatrix}=\begin{pmatrix} 0 \\ 0 \\ 0 \\ \sqrt{2}L \end{pmatrix} \tag{8}$$

The last two sub-equations in Eq. 8 result from the circular restriction and fixed height.

The curled microstructures are simply supported as depicted in Fig. 3 (F and G). According to previous studies (*40*), the governing equation and boundary conditions of the microstructure under horizontal force F_x, vertical force F_y, and moment M_0 at each end can be written as

$$\frac{d^2\psi}{d\alpha^2}=-R\frac{d(R^{-1})}{d\alpha}\left(\frac{d\psi}{d\alpha}-1\right)+R^2\frac{(EA+F_x\cos\psi+F_y\sin\psi)(F_x\sin\psi-F_y\cos\psi)}{EI\cdot EA} \tag{9}$$

$$\frac{d\psi}{d\alpha}(\alpha=\alpha_0)=1 \text{ and } L_y=\int_{\alpha_0}^{\alpha_{end}}(1+\varepsilon)R(\alpha)\sin\psi d\alpha=0 \tag{10}$$

where α and ψ are the undeformed and deformed slope angles, respectively. E is the Young's modulus. A is the cross-sectional area. I is the second area moment, and ε represents the engineering strain at the centroid axis of the infinitesimal curved segment.

The deformed configurations of the microstructures can be calculated by numerical integration with respect to ψ. The deformed length L_i between two ends of the microstructure is given by

$$L_i=\int_{\psi_0}^{\psi_{end}}(1+\varepsilon)R(\psi)\cos\psi d\psi \tag{11}$$

The longitudinal vertical load σ_{zz} and the corresponding reaction force F are obtained by solving Eqs. 4 to 11. The torsional angle φ is calculated by

$$6(L_1\cos\beta_2-L_2\cos\beta_1)=\varphi D/2 \tag{12}$$

Thus, the relationship between T, $F^{\perp}$, and φ can be obtained.

We further extend the theoretical model to the two-segment cylindrical lattice metamaterials. σ_{xz} and σ_{zz} are continuous at the interface of the cylindrical lattice metamaterials (fig. S13). The two segments are individually modeled by Eqs. 4 to 8. The last deformation compatibility equation in Eq. 8 changes to

$$(L_1\sin\beta_2+L_2\sin\beta_1)_{upper}+(L_1\sin\beta_2+L_2\sin\beta_1)_{lower}=2\sqrt{2}L \tag{13}$$

The relationship between σ_{zz} and σ_{xz} can be obtained by solving Eqs. 5 to 8, Eq. 13, and the governing equations of the microstructures. The torsional angle φ is expressed by

$$3(L_1\cos\beta_2-L_2\cos\beta_1)_{upper}+3(L_1\cos\beta_2-L_2\cos\beta_1)_{lower}=\varphi D/2 \tag{14}$$

The applied torque T and the normal force $F^{\perp}$ also satisfy Eq. 4. Thus, the relationship between torque, normal force, and torsional angle can be obtained. The theoretical model for three- or multi-segment cylindrical lattice metamaterials can be derived similarly.

Validation of the theoretical model

Experiments and FE simulations are conducted to validate the theoretical model of cylindrical lattice metamaterials. Two designs are constructed for validation: (i) one segment with all microstructures generated using $R(\alpha)=\alpha$ ($0\le\alpha\le4.5$) (Fig. 4A); and (ii) two segments with the microstructures I and III designed by $R(\alpha)=\alpha^3$ ($0\le\alpha\le3.9$), and microstructures II and IV generated using $R(\alpha)=\alpha$ ($0\le\alpha\le4.5$) (Fig. 4C). All the microstructures are scaled to $L=25\sqrt{2}/2$ mm with width $w=1$ mm and thickness $t=2.5$ mm. The diameter of the lattice metamaterial is 47.75 mm, and the height is 150 mm.

Figure 4 (A and C) shows that the experimental, FE-simulated, and theoretical normal force $F^{\perp}$ and torque T agree well. The details of the characterization and measurements are given in Materials and Method. In Fig. 4A, the single-segment cylindrical lattice metamaterial exhibits a nonreciprocal Poynting effect. When twisted counterclockwise (positive φ), it generates a positive $F^{\perp}$. In contrast, a negative $F^{\perp}$ is formed when twisted clockwise (negative φ). The relationship between $F^{\perp}$ and φ is nonlinear. For example, the cylindrical lattice metamaterial shows a positive $F^{\perp}_{R}=7$ N at $\varphi=\pi/2$ and a larger negative $F^{\perp}_{L}=-12$ N at $\varphi=-\pi/2$. For the two-segment cylindrical lattice metamaterial in Fig. 4C, symmetric negative $F^{\perp}$ manifest, resulting from the opposing arrangement of the two segments. The comparisons between the experimental, FE-simulated, and theoretical shapes of cylindrical lattice metamaterials agree well, as shown in Fig. 4 (B and D). The theoretical deformed shapes are built through a coordinate transformation in three dimensions (fig. S10 and section S8).

The governing equation (Eq. 9) of the microstructure is derived based on the assumption that the material property of the microstructure is linear elastic. This assumption requires that the local strain of the microstructure remains small, even when the cylindrical lattice structures undergo a finite deformation. The FE-simulated strain maps of the deformed cylindrical lattice with a torsional angle $\varphi=\pm\pi/2$ are shown in fig. S12. The strain maps revealed that the local maximum principal strain remains below 4%, validating the assumption of a small local strain.

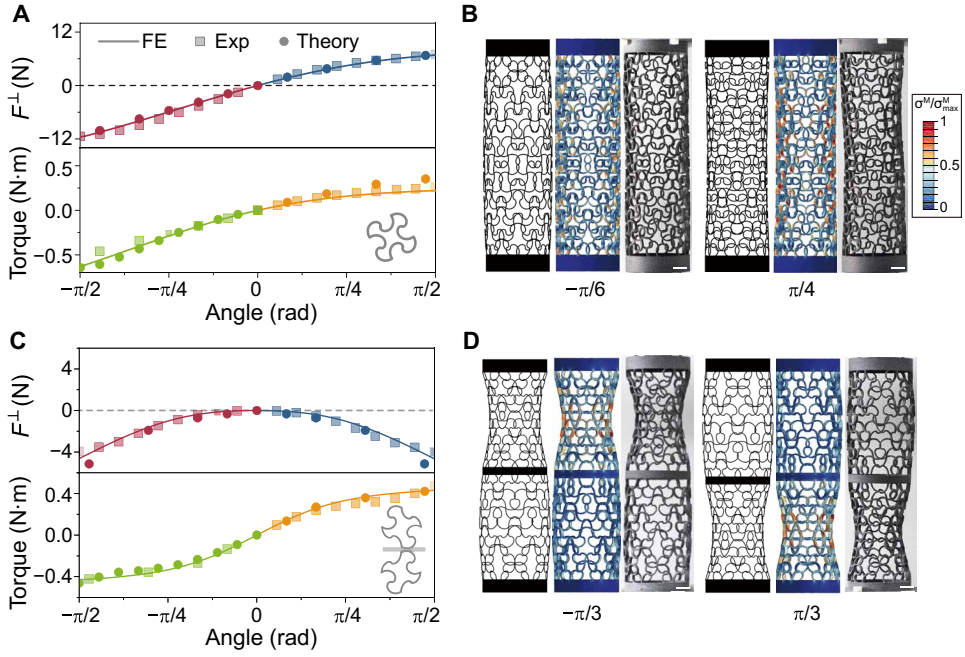

Fig. 4. Theoretical model validation. (**A** and **C**) The experimental, FE-simulated, and theoretical normal force $F^{\perp}$ and torque T versus the torsional angle φ for single-segment and two-segment lattice designs, respectively. The corresponding theoretical deformation, FE simulations, and experimental optical images at specified torsional angles are depicted in (**B**) and (**D**). All scale bars are 10 mm.

Programmable design of the Poynting effect

The validated theoretical model then enables the programmable design of the Poynting effect. By adjusting the lattice configuration and geometric parameters, the Poynting effects can be tuned in all four quadrants: first ($F_L^{\perp} > 0$ and $F_R^{\perp} > 0$), second ($F_L^{\perp} < 0 < F_R^{\perp}$), third ($F_L^{\perp} < 0$ and $F_R^{\perp} < 0$), and fourth ($F_L^{\perp} > 0 > F_R^{\perp}$) (Fig. 5A). For instance, the nonreciprocal Poynting effect in the second quadrant can be obtained (Fig. 5Ba) by using the single-segment cylindrical lattice metamaterial in Fig. 4A. Nonreciprocal Poynting effect that occurs within the fourth quadrant can be generated using the mirrored patterns (Fig. 5Bb). The design space is explored by varying the geometric parameters in section S9.

Two-segment cylindrical lattice metamaterials with opposite segments are used to generate reciprocal Poynting effects. Positive, nearly zero, and negative reciprocal Poynting effects have been designed by adjusting the geometric parameters. For example, when the microstructures I and III are designed by $R(\alpha) = \alpha$ ($0 \le \alpha \le 4.5$) and microstructures II and IV adopt $R(\alpha) = \alpha^3$ ($0 \le \alpha \le 3.9$), a positive reciprocal Poynting effect is formed with normal force at around 4 N at $\varphi = \pm\pi/2$ (Fig. 5Cc). Nearly zero reciprocal Poynting effect is formed when all the microstructures are generated by curvature function $R(\alpha) = \alpha$ ($0 \le \alpha \le 4.5$) (Fig. 5Cd). Using the patterns in Fig. 4C, a negative reciprocal Poynting effect is generated with the normal force at around −4 N when $\varphi = \pm\pi/2$(Fig. 5Ce).

Three-segment cylindrical lattice metamaterials can be used to design the Poynting effect that falls within the first and third quadrants. By adding a segment [microstructures I and III generated by $R(\alpha) = \alpha^3$ ($0 \le \alpha \le 3.9$) and microstructures II and IV using $R(\alpha) = \alpha^2$ ($0 \le \alpha \le 4.1$)] on the two-segment lattice in Fig. 4C, nonreciprocal Poynting effect in the third quadrant is achieved (Fig. 5Df). Various Poynting effect curves in the first and third quadrants can be realized by tuning the geometric parameters of the three-segment patterns (Fig. 5D, g to i).

As the relationship between the geometric parameters and the Poynting effect is nonlinear, obtaining the geometric parameters of a desired Poynting effect is difficult. The optimization method combining machine learning (ML) and evolutionary algorithms (EAs) can be used for fast and efficient inverse design. The ML is used as a surrogated model, while the EA is adopted for fast inverse optimization. Details of the ML-EA methods are shown in section S10.

Bionic Poynting effect matching is demonstrated using the ML-EA method. Bionic Poynting effect matching is essential in tissue engineering and biomedical devices, which can minimize the biological injury caused by the mechanical behavior mismatch (*41*). Polyacrylamide hydrogels and salmon fibrinogen show positive and negative reciprocal Poynting effects, respectively [data from (*24*)]. Using the developed ML-EA method, the optimally designed lattice metamaterials can accurately mimic the Poynting effect of both biological materials. The corresponding periodic units are shown in the inset (Fig. 5D). Section S11 shows another example of designing the nonreciprocal Poynting effect $F_L^{\perp} = -F_R^{\perp}$, i.e., the 135° diagonal line in the second and fourth quadrants.

Application prospects

The design framework allows the one-to-one mapping between the torque and normal forces, which can be used to design soft devices for force transmission. A wave energy converter and unidirectional motion limiter are demonstrated.

Wave energy is a renewable energy source that has attracted substantial interest recently. Current energy-harvesting devices use rigid transmission systems, such as hydraulic systems or gearboxes,

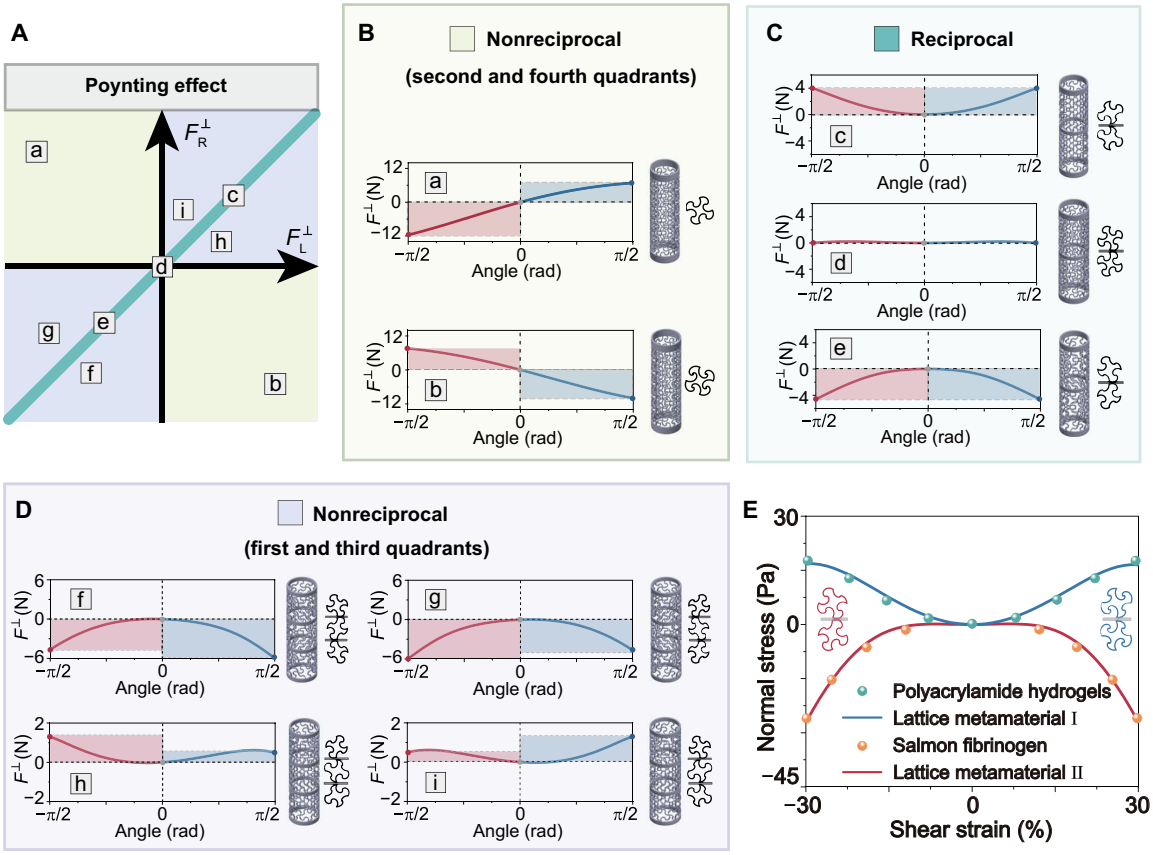

Fig. 5. Programmable design of Poynting effect. (**A**) Design of nonreciprocal and reciprocal Poynting effects using lattice patterns. (**B**) Single-segment cylindrical lattice metamaterials enabled the nonreciprocal Poynting effects in the second and fourth quadrants. (**C**) Two-segment cylindrical lattice metamaterials with opposite segments are used to generate reciprocal Poynting effects. (**D**) Three-segment cylindrical lattice metamaterials can be used to design the Poynting effect that falls within the first and third quadrants. (**E**) Inverse designs of lattice metamaterials demonstrating the bionic Poynting effect matching for both polyacrylamide hydrogels and salmon fibrinogen.

to convert the torque generated by the periodic waves to electricity (*42*, *43*). Here, we demonstrate that using a lattice structure as a mechanism transducer can directly convert the torsion into axial force, and the electric waveform can be tuned. The energy-harvesting device comprises a cylindrical lattice metamaterial, a piezoelectric material, and a capacitor. A stepper motor generates periodic torsion at one end of the cylindrical lattice to simulate the wave-induced torque. An axial force is generated on the other end of the lattice structure due to the Poynting effect. The piezoelectric material converted the axial force to electrical energy for capacitive energy storage (Fig. 6, A and B). Figure 6C demonstrates the generated electrical energy can power a light-emitting diode (movie S1). By tuning the Poynting effect of the metamaterials, diverse electrical signals can be generated to meet specific acquisition requirements. Figure 6D shows the output electric waveform using lattice structures with nonreciprocal or reciprocal Poynting effects.

Figure 6 (E and F) demonstrates the application of the nonreciprocal cylindrical lattice as a unidirectional motion limiter, enabling rotation in one direction while limiting rotation in the opposite direction (movie S2). A lattice metamaterial with $F_L^{\perp} \approx 0$ and $F_R^{\perp} > 0$ is designed. The bottom of the lattice metamaterial is initially immobilized. When the lattice metamaterial undergoes clockwise rotation, no axial deformation occurs as $F_L^{\perp} \approx 0$. The end remains immobilized (Fig. 6E). Conversely, an axial elongation is generated during counterclockwise rotation as $F_R^{\perp} > 0$, releasing the constraint on counterclockwise rotation (Fig. 6F). A real-time monitoring system (section S13 and movie S3) and kinematic controllers (section S13 and movie S4) are also demonstrated using designed nonreciprocal cylindrical lattice. The developed design framework is further extended to metamaterials with 3D lattice units. The FE results show that both reciprocal and nonreciprocal Poynting effects can be realized by designed multi-segment 3D lattice structures (section S12 and fig. S20).

DISCUSSION

The compression-twisting effect is closely related to the Poynting effect. A notable study of the compression-twisting effect comes from Frenzel *et al.* (*20*), who introduced a 3D metamaterial capable of converting unidirectional mechanical input into global twist output, achieving up to 2° per percent of linear deformation. Although the two effects are similar, they are intrinsically different. Both phenomena involve longitudinal and transverse displacements, but the loading condition is different. The displacements

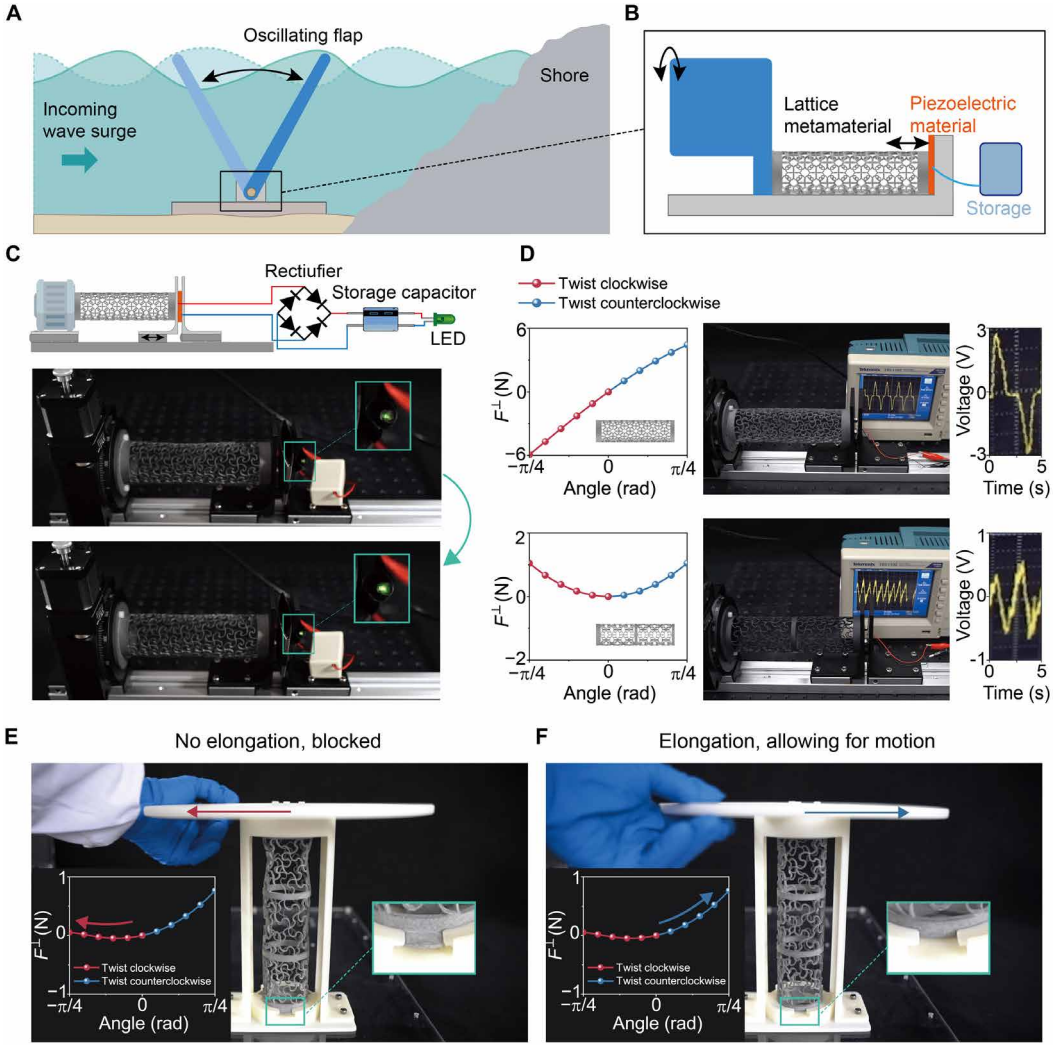

Fig. 6. Application prospects. (**A**) Schematics of wave energy harvesting. (**B**) The energy-harvesting device comprises a cylindrical lattice metamaterial, a piezoelectric material, and a capacitor. (**C**) The generated electrical energy can power a light-emitting diode (LED). (**D**) Different Poynting effects can generate voltage in different forms. The torsion angle–normal force curves and the corresponding voltage waves are shown. (**E** and **F**) A unidirectional motion limiter is designed with $F_L^{\perp} \approx 0$ and $F_R^{\perp} > 0$, which limits the clockwise rotation and allows counterclockwise rotation due to the difference in axial elongation.

are driven by normal force in the compression-twisting effect and by shear force in the Poynting effect (fig. S4A). Detailed force analysis shows that the first-order terms in Poynting and compression-twisting effects are the same, but the second-order terms are different (section S4).

In summary, using a generalized directional truss model, we discover the nonreciprocal Poynting effect, i.e., the normal stresses are unequal for identical shear displacements to the left and right. The truss model further reveals that the material nonlinearity can be used to tune the magnitudes of the nonreciprocal Poynting effect. Inspired by this discovery, we used cylindrical lattice metamaterials constructed from antisymmetric curled microstructures as a case study to generate the nonreciprocal Poynting effect. A design framework that integrates the digital generation, finite deformation theory, FE modeling, and 3D printing fabrication of the cylindrical lattice metamaterial is developed. Reciprocal and nonreciprocal Poynting effects across four quadrants have been programmed using the design framework. The developed method allows the one-to-one mapping between the torque and normal forces, enabling the design of soft devices for force transmission. The practical applications of the Poynting effect were demonstrated with a wave energy converter and unidirectional motion limiter. The developed structures not only can realize conversion between the torque and normal forces but also can provide load-bearing or architectural functions. The design philosophy of embodied energy transmission in structural design paves the way for the design of multifunctional soft devices.

MATERIALS AND METHODS

Automatic digital design workflow

An automatic digital design workflow was developed to obtain the manufacturing representations and program the Poynting effect behaviors of cylindrical lattice metamaterials. It contains the following four steps. First, the microstructures were generated using geometric parameters (n and α_{end}) to form the 2D lattice structures in the algorithmic design environment Rhino Grasshopper. Second,

the cylindrical lattice metamaterials were constructed by wrapping 2D lattice structures into a thin-walled cylinder shape using the 3D modeling software SolidWorks. The stereolithography files were outputted for 3D printing. Next, the theoretical, FE-simulated, and experimental approaches were used to analyze the Poynting effect. Last, the numerical analysis software MATLAB was used to process data and visualization. A homemade Python script was performed to automatically realize the whole workflow by calling the Python Application Programming Interface of the adopted software. The developed workflow avoids complicated structural modeling processes and pre-settings of FE simulations and can be easily combined with the optimization algorithm to obtain desired mechanical responses.

Fabrication

The lattice metamaterials with sophisticated 3D configurations were fabricated using a commercial 3D jetting printer (HP 4200, Hewlett-Packard) based on the Multi Jet Fusion 3D printing technology. Nylon (HP3DHR-PA12, Hewlett-Packard) was chosen as the matrix material with Young's modulus $E = 1.4$ GPa and Poisson's ratio $\nu = 0.4$ (fig. S8 and section S7). The manufactured metamaterials with lattice designs are lightweight (~10 g), enabling them to be supported by leaves, and have high toughness that allows for large deformations without damage (fig. S9).

FE analysis

The commercial FE software ABAQUS (3D Systems, Rock Hill, SC, USA) was used to numerically analyze the Poynting effect of cylindrical lattice metamaterials. The 10-node quadratic tetrahedron element C3D10 was used. Refined meshes were adopted to ensure computational accuracy. The Abaqus/Standard solver was used for quasi-static simulations. The lower surface of the lattice metamaterial was fixed, and torsional boundary conditions were applied to the upper surface while maintaining a constant distance between the two ends. The numerical relationships between torque, torsional angle, and normal force were obtained.

Characterization and measurements

A homemade mechanical testing platform was built to experimentally measure the Poynting effect of lattice metamaterials (fig. S11). An Arduino UNO was used to control a stepper motor (HS2257, Leadshine Co.), combined with a reducer drive module to achieve precise twisting of the metamaterials. A multidimensional force sensor (DYDW-003, Dayang Crop.) was used to collect normal force and torque data simultaneously. All data were transmitted to a host computer and collected in real time using MATLAB (MathWorks).

Supplementary Materials

This PDF file includes:
Section S1 to S13
Figs. S1 to S21
Legends for movies S1 to S4

Other Supplementary Material for this manuscript includes the following:
Movies S1 to S4

REFERENCES AND NOTES

1. J. C. Maxwell, XLV. On reciprocal figures and diagrams of forces. *Lond. Edinb. Dubl. Phil. Mag.* **27**, 250–261 (1864).
2. H. B. G. Casimir, On Onsager's principle of microscopic reversibility. *Rev. Mod. Phys.* **17**, 343–350 (1945).
3. A. Nagulu, N. Reiskarimian, H. Krishnaswamy, Non-reciprocal electronics based on temporal modulation. *Nat. Electron.* **3**, 241–250 (2020).
4. W. Yang, J. Qin, J. Long, W. Yan, Y. Yang, C. Li, E. Li, J. Hu, L. Deng, Q. Du, A self-biased non-reciprocal magnetic metasurface for bidirectional phase modulation. *Nat. Electron.* **6**, 225–234 (2023).
5. Y. Zhang, L. Shi, C. T. Chan, K. H. Fung, K. Chang, Geometrical theory of electromagnetic nonreciprocity. *Phys. Rev. Lett.* **130**, 203801 (2023).
6. B.-I. Popa, S. A. Cummer, Non-reciprocal and highly nonlinear active acoustic metamaterials. *Nat. Commun.* **5**, 3398 (2014).
7. L. Shao, W. Mao, S. Maity, N. Sinclair, Y. Hu, L. Yang, M. Lončar, Non-reciprocal transmission of microwave acoustic waves in nonlinear parity–time symmetric resonators. *Nat. Electron.* **3**, 267–272 (2020).
8. H. Nassar, B. Yousefzadeh, R. Fleury, M. Ruzzene, A. Alù, C. Daraio, A. N. Norris, G. Huang, M. R. Haberman, Nonreciprocity in acoustic and elastic materials. *Nat. Rev. Mater.* **5**, 667–685 (2020).
9. M. Brandenbourger, X. Locsin, E. Lerner, C. Coulais, Non-reciprocal robotic metamaterials. *Nat. Commun.* **10**, 4608 (2019).
10. Y. Zhao, X. Zhou, G. Huang, Non-reciprocal Rayleigh waves in elastic gyroscopic medium. *J. Mech. Phys. Solids* **143**, 104065 (2020).
11. G. Librandi, E. Tubaldi, K. Bertoldi, Programming nonreciprocity and reversibility in multistable mechanical metamaterials. *Nat. Commun.* **12**, 3454 (2021).
12. L. Wang, J. A. I. Martínez, G. Ulliac, B. Wang, V. Laude, M. Kadic, Non-reciprocal and non-Newtonian mechanical metamaterials. *Nat. Commun.* **14**, 4778 (2023).
13. J. Veenstra, O. Gamayun, X. Guo, A. Sarvi, C. V. Meinersen, C. Coulais, Non-reciprocal topological solitons in active metamaterials. *Nature* **627**, 528–533 (2024).
14. C. Coulais, D. Sounas, A. Alu, Static non-reciprocity in mechanical metamaterials. *Nature* **542**, 461–464 (2017).
15. M. Shaat, Nonreciprocal elasticity and the realization of static and dynamic nonreciprocity. *Sci. Rep.* **10**, 21676 (2020).
16. X. Wang, Z. Li, S. Wang, K. Sano, Z. Sun, Z. Shao, A. Takeishi, S. Matsubara, D. Okumura, N. Sakai, Mechanical nonreciprocity in a uniform composite material. *Science* **380**, 192–198 (2023).
17. J. Zhang, M. Xiao, L. Gao, A. Alù, F. Wang, Self-bridging metamaterials surpassing the theoretical limit of Poisson's ratios. *Nat. Commun.* **14**, 4041 (2023).
18. A. Wang, Z. Meng, C. Q. Chen, Non-Hermitian topology in static mechanical metamaterials. *Sci. Adv.* **9**, eadf7299 (2023).
19. J. H. Poynting, On pressure perpendicular to the shear planes in finite pure shears, and on the lengthening of loaded wires when twisted. *Proc. R. Soc. Lond. Ser. A Contain. Pap. Math. Phys. Char.* **82**, 546–559 (1909).
20. T. Frenzel, M. Kadic, M. Wegener, Three-dimensional mechanical metamaterials with a twist. *Science* **358**, 1072–1074 (2017).
21. S. Janbaz, F. Bobbert, M. J. Mirzaali, A. Zadpoor, Ultra-programmable buckling-driven soft cellular mechanisms. *Mater. Horiz.* **6**, 1138–1147 (2019).
22. R. S. Rivlin, Torsion of a rubber cylinder. *J. Appl. Phys.* **18**, 444–449 (1947).
23. L. A. Mihai, A. Goriely, Positive or negative Poynting effect? The role of adscititious inequalities in hyperelastic materials. *Proc. R. Soc. A Math. Phys. Eng. Sci.* **467**, 3633–3646 (2011).
24. P. A. Janmey, M. E. McCormick, S. Rammensee, J. L. Leight, P. C. Georges, F. C. MacKintosh, Negative normal stress in semiflexible biopolymer gels. *Nat. Mater.* **6**, 48–51 (2007).
25. A. Ghorbani, D. Dykstra, C. Coulais, D. Bonn, E. van der Linden, M. Habibi, Inverted and programmable Poynting effects in metamaterials. *Adv. Sci.* **8**, e2102279 (2021).
26. C. O. Horgan, J. G. Murphy, Reverse Poynting effects in the torsion of soft biomaterials. *J. Elast.* **118**, 127–140 (2015).
27. M. Destrade, Y. Du, J. Blackwell, N. Colgan, V. Balbi, Canceling the elastic Poynting effect with geometry. *Phys. Rev. E* **107**, L053001 (2023).
28. J. C. Criscione, I. Lorenzen-Schmidt, J. D. Humphrey, W. C. Hunter, Mechanical contribution of endocardium during finite extension and torsion experiments on papillary muscles. *Ann. Biomed. Eng.* **27**, 123–130 (1999).
29. Z. Liu, M. A. Meyers, Z. Zhang, R. O. Ritchie, Functional gradients and heterogeneities in biological materials: Design principles, functions, and bioinspired applications. *Prog. Mater. Sci.* **88**, 467–498 (2017).
30. R. G. Larson, in *The Structure and Rheology of Complex Fluids* (Oxford Univ. Press, 1999), p. 688.
31. H. C. de Cagny, B. E. Vos, M. Vahabi, N. A. Kurniawan, M. Doi, G. H. Koenderink, F. C. MacKintosh, D. Bonn, Porosity governs normal stresses in polymer gels. *Phys. Rev. Lett.* **117**, 217802 (2016).
32. V. Balbi, A. Trotta, M. Destrade, A. N. Annaidh, Poynting effect of brain matter in torsion. *Soft Matter* **15**, 5147–5153 (2019).
33. J. J. Uicker Jr., G. R. Pennock, J. E. Shigley, *Theory of Machines and Mechanisms* (Cambridge Univ. Press, 2023).

34. C. A. Aubin, B. Gorissen, E. Milana, P. R. Buskohl, N. Lazarus, G. A. Slipher, C. Keplinger, J. Bongard, F. Iida, J. A. Lewis, Towards enduring autonomous robots via embodied energy. *Nature* **602**, 393–402 (2022).
35. C. Horgan, J. Murphy, Fiber-matrix interaction and fiber orientation in simple shearing of fibrous soft tissues. *J. Elast.* **151**, 59–71 (2022).
36. C. Horgan, J. Murphy, Poynting and reverse Poynting effects in soft materials. *Soft Matter* **13**, 4916–4923 (2017).
37. Q. Ma, H. Cheng, K.-I. Jang, H. Luan, K.-C. Hwang, J. A. Rogers, Y. Huang, Y. Zhang, A nonlinear mechanics model of bio-inspired hierarchical lattice materials consisting of horseshoe microstructures. *J. Mech. Phys. Solids* **90**, 179–202 (2016).
38. J. Liu, D. Yan, W. Pang, Y. Zhang, Design, fabrication and applications of soft network materials. *Mater. Today* **49**, 324–350 (2021).
39. A. E. Green, W. Zerna, *Theoretical Elasticity* (Courier Corporation, 1992).
40. D. Wang, L. Dong, G. Gu, 3D printed fractal metamaterials with tunable mechanical properties and shape reconfiguration. *Adv. Funct. Mater.* **33**, 2208849 (2023).
41. F.-M. Chen, X. Liu, Advancing biomaterials of human origin for tissue engineering. *Prog. Polym. Sci.* **53**, 86–168 (2016).
42. A. F. de O. Falcao, Wave energy utilization: A review of the technologies. *Renew. Sustain. Energy Rev.* **14**, 899–918 (2010).
43. Y. Zhang, Y. Zhao, W. Sun, J. Li, Ocean wave energy converters: Technical principle, device realization, and performance evaluation. *Renew. Sustain. Energy Rev.* **141**, 110764 (2021).

Acknowledgments

Funding: D.W. acknowledges support from the National Natural Science Foundation of China (grant no. 52275025), the National Key Research and Development Program of China (no. 2022YFB4700900), and the State Key Laboratory of Mechanical System and Vibration (grant no. MSVZD202301). **Author contributions:** L.D.: Conceptualization, data curation, formal analysis, investigation, methodology, validation, visualization, writing—original draft, and writing—review and editing. K.Z.: Formal analysis, methodology, supervision, validation, visualization, writing—original draft, and writing—review and editing. D.W.: Conceptualization, data curation, formal analysis, funding acquisition, methodology, project administration, resources, software, supervision, validation, visualization, writing—original draft, and writing—review and editing. **Competing interests:** The authors declare that they have no competing interests. **Data and materials availability:** All data needed to evaluate the conclusions in the paper are present in the paper and/or the Supplementary Materials.

Submitted 1 November 2023
Accepted 10 May 2024
Published 14 June 2024
10.1126/sciadv.adl5774